entropy

MDPI

Article

Multi-Field Synergy and Anti-Synergy Mechanisms in Enhanced Heat Transfer Tubes: Angle-Based Characterization and Comprehensive Performance Evaluation

Yanliang Zhang [1,†], Shuo Wang [2,†], Hao Zhang [2], Lin Wan [2,3,*], Chunsheng Wu [4,*], Gang Che [2,3], Hongchao Wang [2,3] and Xilu Li [4]

[1] Heilongjiang Academy of Agricultural Machinery Engineering Sciences, Harbin 150040, China
[2] College of Engineering, Heilongjiang Bayi Agricultural University, Daqing 163319, China
[3] Heilongjiang Provincial Key Laboratory of Intelligent Agricultural Machinery Equipment, Daqing 163319, China
[4] Heilongjiang Academy of Agricultural Machinery Engineering Sciences (Jiamusi Branch), Jiamusi 150086, China
* Correspondence: wanlin163@byau.edu.cn (L.W.); youyouuser94@gmail.com (C.W.); Tel.: +86-178-6024-5596 (L.W.)
† These authors contributed equally to this work.

Abstract

To advance the systematic understanding of synergy and counter-synergy effects in multi-field synergy theory and to address the gap in applications coupling physics-informed neural network methods with multi-field synergy analysis, this study investigates the coupling relationships among vectors in fluid physical fields based on the conservation equations of momentum, energy, and mechanical energy, thereby elucidating the intrinsic connection between multi-field synergy mechanisms and enhanced heat transfer. With a helical groove tube and a novel irregular-shaped tube as the research objects, computational fluid dynamics and a physics-informed neural network were jointly employed to provide an in-depth analysis of synergy and counter-synergy effects in multi-field synergy theory and to quantitatively characterize the synergy effect. On this basis, a comprehensive evaluation criterion grounded in multi-field synergy theory was proposed to assess the overall heat transfer performance of different heat transfer tubes. The results show that, according to the multi-field synergy principle, a clear mapping exists between the multi-field synergy angles and key evaluation indicators, including flow resistance, heat transfer performance, and energy consumption. Moreover, under conditions where experimental validation of field synergy is not feasible, the overall deviation between the field synergy angles reconstructed by the physics-informed neural network and the computational fluid dynamics results was of the order of 10^{-1}, indicating that this method is highly feasible for cross-validation and auxiliary assessment of computational fluid dynamics predictions and can serve as a concise and efficient alternative approach. In addition, the irregular-shaped tube outperformed both the helical groove tube and the smooth circular tube in terms of flow resistance, heat transfer performance, and energy consumption, with the average optimization percentages of the modified performance evaluation coefficient and modified effectiveness evaluation coefficient reaching 2.03% and 7.82%, respectively. This study provides a theoretical basis and an evaluation framework for the enhanced heat transfer design of different heat transfer tubes and demonstrates important practical value.

Check for updates

Academic Editor: Miguel Rubi

Received: 14 October 2026
Revised: 16 November 2026
Accepted: 16 November 2026
Published: 18 November 2026

Copyright: © 2026 by the authors. Licensee MDPI, Basel, Switzerland. This article is an open access article distributed under the terms and conditions of the Creative Commons Attribution (CC BY) license.

Keywords: gas-phase rotary shell-and-tube heat exchanger; helical groove tube; novel irregular-shaped tube; multi-field synergy theory; heat transfer enhancement; physics-informed neural network

1. Introduction

Heat exchangers, as integral components of thermal energy conversion systems, rely heavily on the key heat transfer elements—heat transfer tubes—which play a crucial role in enhancing system performance [1–3]. The gas-phase rotating shell-and-tube heat exchanger, as a novel heat exchange device, utilizes the helical groove tube as its core heat transfer element, which plays a pivotal role in energy conservation and reductions in energy consumption in the food drying process [4]. Developing high-performance non-circular tubes based on enhanced heat transfer mechanisms is one of the most effective ways to improve the efficiency of heat exchangers. In 1998, Guo et al. [5] introduced the principle of field synergy, proposing that the smaller the angle between the velocity gradient and temperature gradient, the more significant the heat transfer effect. He et al. [6] extended this principle to more general transport phenomena and further expanded its applicability to the study of different flow patterns. Additionally, He et al. [7] provided a comprehensive summary of the research progress on the field synergy principle, demonstrating that this theory is applicable not only to parabolic flow but also to elliptical flow.

In recent years, many scholars have used this principle to conduct in-depth analyses of enhanced heat transfer mechanisms in various heat transfer models. For instance, Meng et al. [8] derived a field synergy equation for stable laminar convective heat transfer based on the principle of minimum thermal energy dissipation and designed a new type of enhanced tube based on this equation. Kuo et al. [9] employed two-dimensional numerical simulation to evaluate the convective heat transfer performance of a novel wavy gas flow passage, with results showing that aligning the velocity vector with the temperature gradient is beneficial for enhancing heat transfer performance. Chen et al. [10] used the Lattice Boltzmann method to simulate incompressible low-Reynolds-number flow and verified that the introduction of a cylindrical body that interrupts the flow can reduce the angle between the velocity vector and temperature gradient, thus enhancing heat transfer. Ma et al. [11] validated the second corollary of the field synergy principle through experimental tests on square wind ducts with specially designed wall surfaces, concluding that when the flow direction is perpendicular to the temperature gradient, the heat transfer contribution in the direction of the temperature gradient is zero. Tao et al. [12] systematically analyzed the heat transfer and flow characteristics of corrugated finned tube heat exchangers, evaluating the effects of Reynolds number, fin spacing, wave angle, and tube row number on heat transfer characteristics, and concluded that reducing the angle between the flow velocity and the temperature gradient is an effective way to enhance convective heat transfer characteristics. Furthermore, Tao et al. [13] employed the field synergy principle to simulate and analyze the performance of elliptical tube corrugated fin heat exchangers, validating the feasibility of this principle in enhanced heat transfer design. Chen et al. [14], based on the principle of maximum entropy dissipation, constructed a field synergy equation and found that appropriate internal fins could significantly enhance the fluid synergy effect and improve turbulent heat transfer in turbulent heat transfer tests conducted between parallel plates. Wu et al. [15] used numerical methods to systematically analyze the influence of triangular small wing vortex generators on laminar heat transfer over finned tube surfaces, with results showing that the secondary flows generated by the vortex generators reduce the angle between the velocity gradient and temperature gradient, revealing the intrinsic mechanism of heat transfer enhancement. Cheng et al. [16] performed numerical

simulations to analyze the coupled heat transfer process in electronic cooling and used the field synergy principle to investigate the coupling mechanism of fluid flow and heat transfer, proposing corresponding optimization design methods. Wu and Tao et al. [17] systematically analyzed the laminar convective heat transfer characteristics of channels with longitudinal vortex generators, verifying the applicability of the field synergy principle in these structures. Chang et al. [18] introduced wavy and circular obstacles in Y-shaped channels and systematically analyzed the effect of the arrangement of these obstacles on heat transfer efficiency using the field synergy principle. Their results indicated that heat transfer efficiency is closely related to the angle between the velocity vector and the temperature gradient within the channel. Guo et al. [19] applied the field synergy principle to optimize the shell-side and tube-side designs of heat exchangers, using the maximum field synergy number as the objective function and employing a genetic algorithm for optimization, resulting in significantly improved heat exchanger performance. Gou et al. [20] analyzed the relationship between overall and local field synergy in a two-dimensional convection heat transfer experiment under conditions of parallel permeable wall designs, concluding that the local field synergy is more practical than the overall field synergy under certain conditions. Guo et al. [21] conducted a computational fluid dynamics analysis on the fluid flow and heat transfer characteristics in pipes with helical strips and used the field synergy principle to explain the mechanism of heat transfer enhancement by spiral baffle inserts: the smaller the angle between the temperature gradient and the velocity vector, the higher the Nusselt number. Li et al. [22] performed field synergy analysis on triangular-hole fins, providing a new theoretical framework for fin structure design. Hua et al. [23] proposed a new optimization method based on energy conservation, using extended energy transfer to optimize one-dimensional transient heat conduction problems, providing a theoretical basis for minimizing energy losses in heat transfer processes. Mehra et al. [24] used the field synergy theory to analyze the convective heat transfer characteristics of different planar fin configurations, with results indicating that optimized fin designs can effectively improve heat transfer performance, and the synergy between the velocity field and temperature field significantly influences heat transfer effects. Zhang et al. [25] systematically studied the heat transfer enhancement and flow characteristics of cosine-shaped flow passages, using the field synergy principle to analyze the cooperative effect of temperature and velocity gradients inside the passage, revealing the significant promotion effect of fluid disturbances on heat transfer efficiency. Zuo et al. [26] studied the coupling characteristics of flow fields and temperature fields in electric heating catalytic converters based on the field synergy principle, verifying that the field synergy strategy can effectively improve system thermal efficiency. Hao et al. [27] optimized the channel structure of proton exchange membrane fuel cells based on finite data mapping and multi-field synergy principles, showing that the optimized channel structure significantly improves heat transfer efficiency and energy conversion efficiency.

In summary, existing studies have confirmed the effectiveness of the multi-field synergy theory in enhanced heat transfer, indicating that this theory is supported by a relatively solid research foundation. However, prior work has mainly focused on applying this theory to heat transfer models and evaluating their heat transfer performance, whereas in-depth investigation of the theory itself remains limited, particularly with respect to the systematic elucidation of synergy and counter-synergy effects. In addition, studies that couple the physics-informed neural network (PINN) with physical fields such as the temperature field, velocity field, and pressure field and apply it to heat transfer models are still scarce, and the corresponding methodological framework remains underdeveloped.

This study analyzes the coupling relationships among vectors in fluid physical fields on the basis of the conservation equations of momentum, energy, and mechanical energy, thereby elucidating the intrinsic connection between the multi-field synergy law and the mechanism of enhanced heat transfer. With the helical groove tube and the novel irregular-shaped tube as the research objects, computational fluid dynamics (CFD) and physics-informed neural network methods are employed in combination to provide an in-depth investigation of synergy and counter-synergy effects in multi-field synergy theory and to quantitatively characterize the synergy effect. On this basis, a comprehensive evaluation criterion grounded in multi-field synergy theory is proposed to assess the overall heat transfer performance of different heat transfer tubes.

2. Research Methodology

2.1. Description of Multi-Field Synergy Theory

To characterize the coupled behaviors of flow resistance–heat transfer–energy consumption inside a helical groove tube within the framework of the multi-field synergy theory, this study takes as its core the angles between the velocity vector U and the gradient vectors (velocity gradient ∇u, temperature gradient ∇T, and pressure gradient ∇p). Accordingly, three synergy angles—α, β, and θ—are established to characterize the directional relationships among the velocity field and the corresponding physical fields.

The momentum synergy angle α, defined through the synergy between U and ∇u, quantifies the degree of coupling between the main-flow direction and the momentum diffusion direction [28–30]. According to the vector dot–product relationship (see Equation (1)), a larger α indicates a more pronounced deviation between the main flow and the direction of momentum diffusion, implying a weakened viscous-related hindrance effect associated with momentum diffusion. This is usually accompanied by a lower required pressure gradient and reduced frictional resistance. Therefore, α can serve as an indicator of the internal flow resistance level: a larger α corresponds to a "smoother" flow and a lower flow resistance.

$$U \cdot \nabla U = |U||\nabla U| cos\alpha \tag{1}$$

The heat transfer synergy angle β, defined through the synergy between U and ∇T, describes the coordination level between the convective heat-carrying direction of the main flow and the direction of the temperature gradient [28,31–34]. A smaller β means that the effective component of the temperature gradient along the main-flow direction is larger, leading to more sufficient convective heat transport, which typically manifests as increases in the Nusselt number and the heat transfer coefficient. According to the vector dot–product relationship (see Equation (2)), β can be used as an indicator of heat transfer performance: a smaller β implies stronger coupling between heat flux and mass flow and thus better heat transfer effectiveness.

$$U \cdot \nabla T = |U||\nabla T| cos\beta \tag{2}$$

The power consumption synergy angle θ, defined through the synergy between U and ∇p, characterizes the matching efficiency between the pressure-driving direction and the velocity response [28,35–39]. The corresponding vector dot–product relationship is shown in Equation (3). Thus, θ characterizes the directional matching between the velocity field and pressure gradient field. When the magnitudes of U and ∇p are fixed, a smaller θ corresponds to a larger $\cos\theta$, indicating stronger directional alignment between the velocity and pressure gradient vectors. This relationship provides a basis for characterizing the synergy between pressure driving and fluid motion. Under the operating conditions investigated in this

study, the variation in θ is further evaluated together with the calculated pressure drop and energy consumption characteristics.

$$U \cdot \nabla p = |U||\nabla p| \cos\theta \tag{3}$$

Therefore, the three synergy angles provide geometric measures of the directional relationships among different physical fields from the perspectives of momentum transport, thermal transport, and pressure-driven flow. It should be emphasized that these synergy angles primarily characterize the directional coupling between physical fields, whereas the magnitudes of the corresponding physical quantities and their gradients determine the intensity of the associated transport processes. Consequently, the relationships between the synergy angles and macroscopic performance parameters, such as flow resistance, heat transfer performance, and energy consumption, should be interpreted in conjunction with the governing equations and specific operating conditions rather than regarded as unconditional one-to-one causal relationships. The calculation formulas of α, β, and θ are given in Equation (4). The definition of the above synergy angle metrics depends on the spatial scope of the object under investigation: volume-averaged values are adopted to characterize the overall behavior of the entire fluid domain, whereas area-averaged values are used to characterize the behavior of a given cross-section or specific plane.

$$\begin{cases} \alpha = \frac{180}{\pi} \cdot cos^{-1}\left(\frac{U \cdot \nabla u}{|U||\nabla u|}\right) \\ \beta = \frac{180}{\pi} \cdot cos^{-1}\left(\frac{U \cdot \nabla T}{|U||\nabla T|}\right) \\ \theta = \frac{180}{\pi} \cdot cos^{-1}\left(\frac{U \cdot \nabla p}{|U||\nabla p|}\right) \end{cases} \tag{4}$$

It should be noted that the modified synergy angle is a geometric measure of the directional relationship between the relevant physical field vectors. Its magnitude should not be interpreted as a direct substitute for the corresponding macroscopic performance parameter. In particular, the actual energy consumption should be determined from the calculated pressure drop or pumping power requirement.

2.2. CFD Method Description

Computational fluid dynamics (CFD) is employed to analyze fluid flow and heat transfer processes through numerical simulation. Figure 1 shows the gas-phase rotating shell-and-tube heat exchanger independently developed by our team [40], with the helical groove tube as the core heat transfer element. This study focuses on the helical groove tube, optimizing the design based on the Nusselt number (Nu) and pressure drop (ΔP). Optimization is performed using Parameter Estimation (PE) and Continuous Adjoint Optimization (CADJ). The detailed optimization procedure follows previous work [41] and is therefore not repeated here. The result is a novel, high-efficiency shaped tube that retains the basic structure of the helical groove tube while improving its surface morphology. This paper conducts a multi-field collaborative principal analysis for both tube types. Due to the difficulty in directly analyzing the inner wall of the tube, this study instead analyzes the fluid column and its surface, indirectly substituting the investigation of the inner wall morphology, as shown in Figure 2. Since the original dimensions of the heat exchange tube are relatively large, a tube with an effective length of 1000 mm (L_{eff}) is selected for numerical simulation, with specific structural dimensions provided in Table 1. Air at a temperature of 280.36 K is chosen as the working fluid, with its physical properties listed in Table 2. The numerical domain is the internal air passage of a single tube with an effective length of 1000 mm. The model assumes a stationary tube and a spatially uniform wall temperature. Shell-side flow, tube rotation, and interactions among tubes in a bundle are outside the computational domain. The comparison therefore concerns internal flow and heat transfer in the modeled tubes under the prescribed operating conditions.

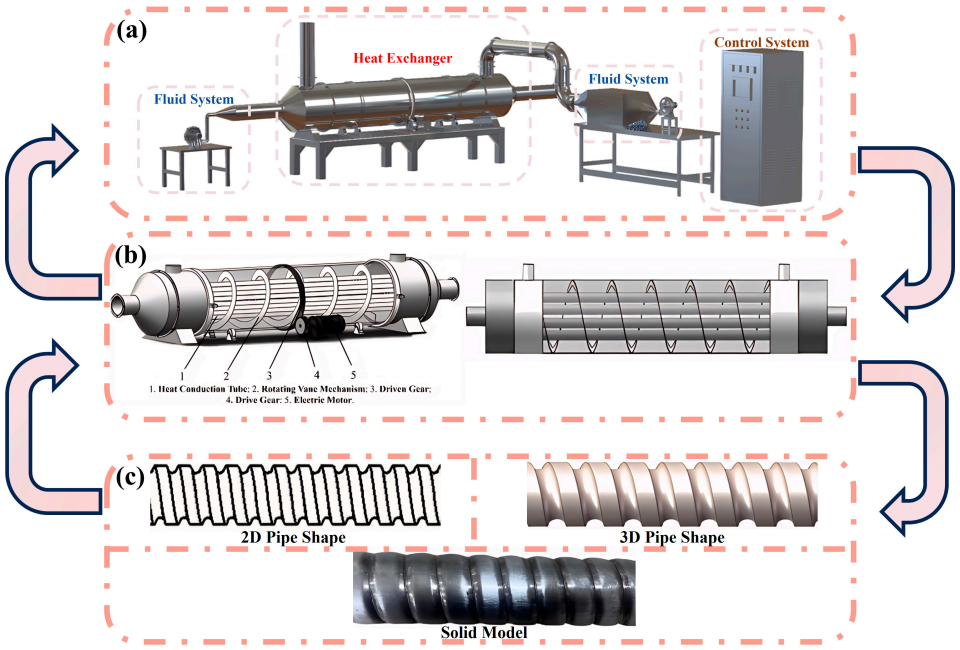


Figure 1. Heat exchanger testing platform: (**a**) system structure of platform; (**b**) 3D full and simplified models of heat exchanger; (**c**) geometric model of helical groove tube.

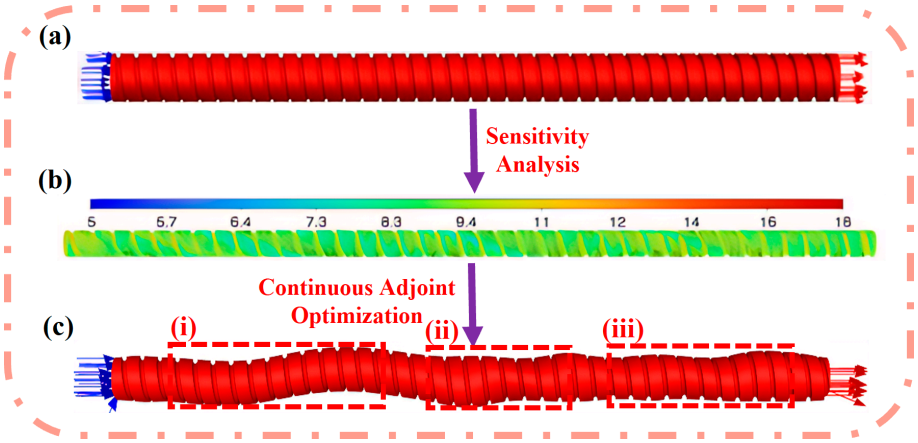


Figure 2. Continuous adjoint optimization process and morphological changes of fluid column before and after optimization: (**a**) original fluid column model; (**b**) sensitivity analysis of *Nu* and Δ*P* values; (**c**) optimized fluid column model.

Table 1. Geometric and structural parameters of helical groove tube.

Number of Grooves n	Inner Diameter of the Groove Tube d_{in}/mm	Outer Diameter of the Groove Tube d_{out}/mm	Groove Width w/mm	Groove Depth e/mm	Pitch p/mm	Helix β''/°
1	38.00	42.00	6.20	3.10	25.23	8.62

Table 2. Thermophysical properties of working fluid.

Working Medium	Fluid Density ρ/kg·m^{-3}	Specific Heat Capacity c_p/J (kg·K)$^{-1}$	Thermal Conductivity λ/W·(m·K)$^{-1}$	Viscosity Coefficient μ/Pa·s
air	1.225	1.006×10^3	2.42×10^{-2}	1.789×10^{-5}

Air was modeled as an incompressible Newtonian fluid with constant properties. The model assumes forced turbulent convection and neglects gravity, buoyancy, volumetric heat generation, and radiation. The inlet velocity (5.30 m s^{-1}), inlet temperature (280.36 K), and wall temperature (352.82 K) were taken from the parameter combination identified in the preceding PE/CADJ design study [41] and reported in Section 3.2. Applying the same values to the three geometries provides a common basis for comparison. The inlet was prescribed by velocity and temperature, the outlet gauge pressure was set to 0.00 Pa, and the stationary wall was modeled as impermeable and no-slip at a uniform temperature. The prescribed wall-to-inlet temperature difference was 72.46 K. The steady three-dimensional governing equations were discretized with the finite-volume method using second-order upwind schemes, the k–ω SST turbulence model, and a coupled pressure–velocity solution. The Fluent residual-monitor thresholds were 10^{-8} for energy and 10^{-6} for the remaining equations. These thresholds apply to the residuals of the discrete CFD equations. The PINN optimizer uses a separate stopping criterion based on the relative change in its training loss, as described in Section 2.4.

Mesh sensitivity was assessed with unstructured tetrahedral meshes. The changes in the monitored fluid temperature and inlet mass flow rate decreased as the mesh was refined from 0.55 million to 1.86 million cells. The final mesh contained approximately 2.00 million cells after local refinement. Table 3 reports the mesh comparison. Table 4 reports differences between the simulated Nu values and those calculated using the Gnielinski correlation in Equation (5). The reported differences are below 5.00% over the Reynolds numbers listed. The correlation was developed for smooth tubes, so this comparison provides a reference check on the magnitude and trend of Nu. Validation of the two profiled geometries requires measurements for those geometries.

$$\begin{cases} Nu = 0.0214\left(Re^{0.8} - 100\right)Pr^{0.4}\left[1 + (d_e/L_{\text{eff}})^{2/3}\right](T_{\text{m}}/T_{\text{wall}})^{0.45} \\ 0.6 < Pr < 1.5,\ 0.5 < T_{\text{m}}/T_{\text{wall}} < 1.5,\ 2300 < Re < 10^6 \end{cases} \quad (5)$$

Table 3. Grid independence test.

Number of Mesh Elements	Novel Irregular-Shaped Tube				Helical Groove Tube			
	T^{n}_{fluid} /K	$\lvert(T^{1.5n}_{fluid}-T^{n}_{fluid})/T^{n}_{fluid}\rvert$ /%	$\dot{m}^{n}_{inlet}$ /kg·s^{-1}	$\lvert(\dot{m}^{1.5n}_{inlet}-\dot{m}^{n}_{inlet})/\dot{m}^{n}_{inlet}\rvert$ /%	T^{n}_{fluid} /K	$\lvert(T^{1.5n}_{fluid}-T^{n}_{fluid})/T^{n}_{fluid}\rvert$ /%	$\dot{m}^{n}_{inlet}$ /kg·s^{-1}	$\lvert(\dot{m}^{1.5n}_{inlet}-\dot{m}^{n}_{inlet})/\dot{m}^{n}_{inlet}\rvert$ /%
5.5×10^5	328.137	–	0.00278	–	321.141	–	0.00235	–
8.3×10^5	324.021	1.25	0.00267	3.96	318.697	0.76	0.00225	4.26
1.24×10^6	321.324	0.83	0.00259	3.00	317.524	0.37	0.00227	0.89
1.86×10^6	321.493	0.05	0.00258	0.39	317.442	0.03	0.00226	0.44

Table 4. Comparison of simulated Nusselt numbers with correlation values.

Reynolds Number	Novel Irregular-Shaped Tube				Helical Groove Tube			
	Theoretical *Nu*	Simulated *Nu*	Absolute *Nu* Difference	Percentage Difference /%	Theoretical *Nu*	Simulated *Nu*	Absolute *Nu* Difference	Percentage Difference /%
6383.324	8.181	8.328	0.147	1.80	5.076	5.213	0.137	2.70
10,554.827	11.717	11.260	0.457	3.90	9.841	10.114	0.273	2.77
14,143.432	16.537	16.950	0.413	2.50	12.986	13.098	0.112	0.86
17,463.257	21.984	21.083	0.901	4.10	15.712	16.094	0.382	2.43
21,259.586	27.352	27.680	0.328	1.20	17.944	18.387	0.443	2.47
25,025.621	32.007	30.951	1.056	3.30	21.026	21.312	0.286	1.36
28,216.227	35.331	36.744	1.413	4.00	23.535	24.047	0.512	2.18
33,989.439	37.971	37.174	0.797	2.10	26.851	27.348	0.497	1.85

This study focuses on the detailed fluid flow characteristics in the near-wall region, where local mesh refinement is applied. Given the complex velocity and temperature distributions at the inlet and outlet, along with significant variations in the boundary layers of both the flow and thermal fields, further mesh refinement is required to create a dense grid in this area. The base grid size is set to 0.10 mm, suitable for the primary mesh, with boundary layer meshes on the wall consisting of five layers. The first mesh layer thickness is 0.01 mm, with a growth factor of 1.15, resulting in the final mesh layer thickness of 0.0175 mm near the wall. The numerical model is shown in Figure 3. The dimensionless parameter y^+, defined by Equation (6), characterizes the distance from the viscous sublayer to the wall, where Δy represents the distance from the first mesh layer to the wall, and τ_{wall} denotes the wall shear stress [42–46]. Figure 3a,b present the y^+ distributions along the inner walls of the two heat exchanger tubes. For the novel irregular-shaped tube, y^+ varies from 0.01 to 6.47, with a maximum of 6.47 and a mean of 3.13; for the helical groove tube, y^+ ranges from 0.07 to 4.79, with a maximum of 4.79 and a mean of 2.15. These results meet the near-wall mesh resolution requirements. The mesh quality is excellent, with a minimum orthogonality of 0.34 and 0.31, maximum skewness of 0.46 and 0.48, peak aspect ratio of 23.18 and 22.86, adjacent-cell volume ratio of 1.23 and 1.27, and a growth rate of 1.15. All parameters meet the boundary-layer mesh generation requirements (orthogonality ≥ 0.3, skewness ≤ 0.5, volume ratio ≤ 1.3), ensuring the stability and accuracy of the numerical simulations.

$$y^+ = \frac{\Delta y \rho}{\mu} \cdot \sqrt{\frac{\tau_w}{\rho}} \tag{6}$$

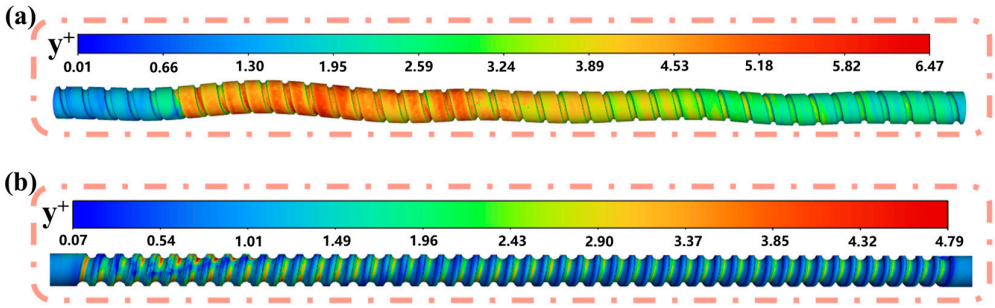


Figure 3. y^+ distribution of numerical models: (**a**) the novel irregular-shaped tube; (**b**) the helical groove tube.

2.3. Description of Multi-Field Synergy Method

In the CFD analysis, this study qualitatively and quantitatively investigates the flow resistance synergy angle α, heat transfer synergy angle β, and power consumption synergy angle θ through field functions. However, due to the three-dimensional turbulent state of the fluid inside the tube, the field functions employed differ from the standard formulas in multi-field synergy theory. To balance directional accuracy and numerical stability, both the standard synergy angle formula (without absolute value) and the modified formula (with absolute value) are used for analysis. The standard formula reveals the "anti-synergy" phenomenon in the flow field, which refers to the negative correlation between the flow direction and the gradients of other physical quantities, while the modified formula effectively avoids negative values, making it easier to compare the degree of synergy across different structures.

Specifically, the standard synergy angle formula calculates the angle between the flow direction and the gradients of velocity, temperature, and pressure via the dot product. In contrast, the modified formula takes the absolute value of the dot product result to eliminate the effect of negative values, ensuring the angle always remains between 0° and 90°, thus providing a consistent measure of synergy. Under three-dimensional turbulent conditions, the modified formulas for flow resistance synergy angle α', heat transfer synergy angle β', and power consumption synergy angle θ' are shown in Equation (7).

$$\alpha' = \frac{180}{\pi}\cdot cos^{-1}\left(\frac{|U\cdot\nabla u|}{|U||\nabla u|}\right),\ \beta' = \frac{180}{\pi}\cdot cos^{-1}\left(\frac{|U\cdot\nabla T|}{|U||\nabla T|}\right),\ \theta' = \frac{180}{\pi}\cdot cos^{-1}\left(\frac{|U\cdot\nabla p|}{|U||\nabla p|}\right) \quad (7)$$

The standard synergy angle and the modified synergy angle were appropriately reformulated to derive field function expressions compatible with ANSYS Fluent 2024 R2 software, as given in Equations (8) and (9).

$$\begin{cases} \alpha = \frac{180}{\pi}\cdot cos^{-1}\left(\frac{U\cdot\nabla u}{|U||\nabla u|}\right) = \frac{180}{\pi}\cdot \\ cos^{-1}\left(\frac{V_x\cdot\left(V_x\cdot\frac{\partial V_x}{\partial x}+V_y\cdot\frac{\partial V_y}{\partial x}+V_z\cdot\frac{\partial V_z}{\partial x}\right)+V_y\cdot\left(V_x\cdot\frac{\partial V_x}{\partial y}+V_y\cdot\frac{\partial V_y}{\partial y}+V_z\cdot\frac{\partial V_z}{\partial y}\right)+V_z\cdot\left(V_x\cdot\frac{\partial V_x}{\partial z}+V_y\cdot\frac{\partial V_y}{\partial z}+V_z\cdot\frac{\partial V_z}{\partial z}\right)}{\sqrt{V_x^2+V_y^2+V_z^2}\cdot\sqrt{\left(V_x\cdot\frac{\partial V_x}{\partial x}+V_y\cdot\frac{\partial V_y}{\partial x}+V_z\cdot\frac{\partial V_z}{\partial x}\right)^2+\left(V_x\cdot\frac{\partial V_x}{\partial y}+V_y\cdot\frac{\partial V_y}{\partial y}+V_z\cdot\frac{\partial V_z}{\partial y}\right)^2+\left(V_x\cdot\frac{\partial V_x}{\partial z}+V_y\cdot\frac{\partial V_y}{\partial z}+V_z\cdot\frac{\partial V_z}{\partial z}\right)^2}}\right) \\ \beta = \frac{180}{\pi}\cdot cos^{-1}\left(\frac{U\cdot\nabla T}{|U||\nabla T|}\right) = \frac{180}{\pi}\cdot cos^{-1}\left(\frac{V_x\cdot\frac{\partial T}{\partial x}+V_y\cdot\frac{\partial T}{\partial y}+V_z\cdot\frac{\partial T}{\partial z}}{\sqrt{V_x^2+V_y^2+V_z^2}\cdot\sqrt{\left(\frac{\partial T}{\partial x}\right)^2+\left(\frac{\partial T}{\partial y}\right)^2+\left(\frac{\partial T}{\partial z}\right)^2}}\right) \\ \theta = \frac{180}{\pi}\cdot cos^{-1}\left(\frac{U\cdot\nabla p}{|U||\nabla p|}\right) = \frac{180}{\pi}\cdot cos^{-1}\left(\frac{V_x\cdot\frac{\partial p}{\partial x}+V_y\cdot\frac{\partial p}{\partial y}+V_z\cdot\frac{\partial p}{\partial z}}{\sqrt{V_x^2+V_y^2+V_z^2}\cdot\sqrt{\left(\frac{\partial p}{\partial x}\right)^2+\left(\frac{\partial p}{\partial y}\right)^2+\left(\frac{\partial p}{\partial z}\right)^2}}\right) \end{cases} \quad (8)$$

$$\begin{cases} \alpha' = \frac{180}{\pi}\cdot cos^{-1}\left(\frac{|U\cdot\nabla u|}{|U||\nabla u|}\right) = \frac{180}{\pi}\cdot \\ cos^{-1}\left(\frac{\left|V_x\cdot\left(V_x\cdot\frac{\partial V_x}{\partial x}+V_y\cdot\frac{\partial V_y}{\partial x}+V_z\cdot\frac{\partial V_z}{\partial x}\right)+V_y\cdot\left(V_x\cdot\frac{\partial V_x}{\partial y}+V_y\cdot\frac{\partial V_y}{\partial y}+V_z\cdot\frac{\partial V_z}{\partial y}\right)+V_z\cdot\left(V_x\cdot\frac{\partial V_x}{\partial z}+V_y\cdot\frac{\partial V_y}{\partial z}+V_z\cdot\frac{\partial V_z}{\partial z}\right)\right|}{\sqrt{V_x^2+V_y^2+V_z^2}\cdot\sqrt{\left(V_x\cdot\frac{\partial V_x}{\partial x}+V_y\cdot\frac{\partial V_y}{\partial x}+V_z\cdot\frac{\partial V_z}{\partial x}\right)^2+\left(V_x\cdot\frac{\partial V_x}{\partial y}+V_y\cdot\frac{\partial V_y}{\partial y}+V_z\cdot\frac{\partial V_z}{\partial y}\right)^2+\left(V_x\cdot\frac{\partial V_x}{\partial z}+V_y\cdot\frac{\partial V_y}{\partial z}+V_z\cdot\frac{\partial V_z}{\partial z}\right)^2}}\right) \\ \beta' = \frac{180}{\pi}\cdot cos^{-1}\left(\frac{|U\cdot\nabla T|}{|U||\nabla T|}\right) = \frac{180}{\pi}\cdot cos^{-1}\left(\frac{\left|V_x\cdot\frac{\partial T}{\partial x}+V_y\cdot\frac{\partial T}{\partial y}+V_z\cdot\frac{\partial T}{\partial z}\right|}{\sqrt{V_x^2+V_y^2+V_z^2}\cdot\sqrt{\left(\frac{\partial T}{\partial x}\right)^2+\left(\frac{\partial T}{\partial y}\right)^2+\left(\frac{\partial T}{\partial z}\right)^2}}\right) \\ \theta' = \frac{180}{\pi}\cdot cos^{-1}\left(\frac{|U\cdot\nabla p|}{|U||\nabla p|}\right) = \frac{180}{\pi}\cdot cos^{-1}\left(\frac{\left|V_x\cdot\frac{\partial p}{\partial x}+V_y\cdot\frac{\partial p}{\partial y}+V_z\cdot\frac{\partial p}{\partial z}\right|}{\sqrt{V_x^2+V_y^2+V_z^2}\cdot\sqrt{\left(\frac{\partial p}{\partial x}\right)^2+\left(\frac{\partial p}{\partial y}\right)^2+\left(\frac{\partial p}{\partial z}\right)^2}}\right) \end{cases} \quad (9)$$

2.4. Physics-Informed Neural Network Validation Method

Because the novel irregular-shaped tube is difficult to manufacture using conventional rolling processes, it is typically fabricated by 3D printing in engineering practice. However, 3D printing is costly, and its metallurgical microstructure differs markedly from that produced by rolling, which may lead to material properties deviating from those under actual service conditions. In addition, due to limitations of the experimental platform, in-tube flow and heat transfer tests cannot be directly conducted on the heat exchanger rig (see Figure 1). A physics-informed neural network (PINN) was used to reconstruct the synergy angle distributions on a two-dimensional longitudinal section. The PINN was selected because it provides a continuous spatial representation of the angle fields and allows equation residuals and CFD-derived boundary samples to be incorporated into the training. The reconstructed values were compared with the CFD results at 500 sampled coordinates to assess agreement with the CFD reference. Because the two approaches share physical modeling assumptions and the PINN uses CFD-derived boundary samples, systematic errors in the CFD model can carry over to the reconstruction. The agreement therefore describes reconstruction consistency at the sampled locations under the adopted modeling assumptions. When constructing the PINN framework, the physical process is

first formulated in a form suitable for neural network training. For heat transfer problems, the physical fields are typically governed by partial differential equations (PDEs).

Within the PINN framework, a surrogate model for the synergy angle field is developed based on the two-dimensional coordinates of the XY longitudinal section of the irregular-shaped tube and the parameters in the governing equations for flow, heat transfer, and energy. Let the target synergy angle field be $\phi \in \{\alpha,\beta,\theta\}$ (or $\phi' \in \{\alpha',\beta',\theta'\}$), which satisfies the PDE operator $g(\cdot)$ constructed by coupling the momentum equations, the energy equation, and the defining expressions of the synergy angles (see Equation (10)).

$$g(\phi) = 0 \tag{10}$$

The PINN takes $\phi(x,y,\vartheta)$ as inputs and outputs an approximation $\phi_0(x,y,\vartheta)$ through a fully connected neural network. Automatic differentiation is employed to compute the spatial derivatives of ϕ_0, thereby forming the equation residual $g(\phi_0)$. Using the interior residual as the primary loss term, the network weights w and biases b are iteratively updated via gradient descent, yielding $\phi(x,y,\vartheta)$ as the PINN approximation of $\phi^0(x,y,\vartheta)$. The forward propagation is given by Equation (11), where l denotes the layer index, i and j are neuron indices, and $\sigma(\cdot)$ is the Sigmoid activation function.

$$\begin{cases} \phi(x,y,\vartheta) \in \{\alpha(x,y,\vartheta),\ \beta(x,y,\vartheta),\ \theta(x,y,\vartheta)\}\ or\ \phi(x,y,\vartheta) \in \{\alpha'(x,y,\vartheta),\ \beta'(x,y,\vartheta),\ \theta'(x,y,\vartheta)\} \\ a_j^l(x,y,\vartheta) = \sigma\left(\sum_i w_{ji}^l a_i^{l-1}(x,y,\theta) + b_j^l\right) \\ \phi(x,y,\vartheta) = a^L(x,y,\vartheta;w,b) \end{cases} \tag{11}$$

Considering that the internal flow is turbulent, the momentum transport is governed by the N—S equations, and turbulence effects are described using the k–ω SST turbulence model. In addition to the velocity field u, the transport equations for the turbulent kinetic energy k and the specific dissipation rate ω are solved, as shown in Equation (12). Here, $\nabla\cdot(\mu_T(\nabla u + (\nabla u)^T))$ denotes the divergence of the viscous stress term, P_k is the production term of turbulent kinetic energy, β^* is a model constant, and γ and δ are constants related to the dissipation terms.

$$\begin{cases} \rho\left(\frac{\partial u}{\partial t} + u\cdot\nabla u\right) = -\nabla p + \nabla\cdot\left(\mu_T\left(\nabla u + (\nabla u)^T\right)\right) \\ \frac{\partial k}{\partial t} + u\cdot\nabla k = \nabla\cdot(\mu_T\nabla k) + P_k - \beta^*\rho\omega k \\ \frac{\partial \omega}{\partial t} + u\cdot\nabla\omega = \nabla\cdot(\mu_T\nabla\omega) + \gamma\frac{\omega k}{\mu_T} - \delta\omega^2 \end{cases} \tag{12}$$

Heat transfer, accounting for both convection and conduction, is governed by the energy equation given in Equation (13).

$$\rho C_p u\frac{\partial T}{\partial x} - \lambda\left(\frac{\partial^2 T}{\partial x^2} + \frac{\partial^2 T}{\partial y^2}\right) = 0 \tag{13}$$

In the two-dimensional PINN domain, the upper and lower boundaries at $y = \pm R$ are treated as adiabatic. A homogeneous Neumann condition is imposed on these boundaries to prescribe zero normal conductive heat flux, as expressed in Equation (14). Here, $(\partial T/\partial y)$ denotes the temperature gradient normal to the boundaries, and R is the distance from the centerline to either boundary.

$$\frac{\partial T}{\partial y} = 0, y = \pm R \tag{14}$$

At the inlet, a prescribed Dirichlet boundary condition T_{in} is applied. Moreover, to enforce boundary conditions strictly within the PINN framework via a hard-constraint strategy, a boundary function $G(x,y,\vartheta)$ and a distance function $D(x,y,\vartheta)$ are introduced, and a boundary-satisfying trial solution $h(x,y,\vartheta)$ is constructed, as shown in

Equations (15) and (16). In these equations, L is the computational domain length and a_L is the network output term.

$$G(x, y, \vartheta) = T_{in},\ D(x, y, \vartheta) = x/L \tag{15}$$

$$h(x, y, \vartheta) = T_{in} + (x/L) \cdot a_L(x, y, \vartheta; w, b) \tag{16}$$

The hard-constraint strategy embeds the boundary conditions directly into the solution structure and avoids reliance on empirical penalty coefficients, thereby suppressing non-physical solutions. In addition, boundary sample data of the synergy angles are used for training, and the physical constraints of the k—ω SST turbulence model are incorporated into the PINN surrogate to ensure that turbulent physics and energy transport are properly embedded in the network. The total loss function $Loss_{\text{hard}}$ is given in Equation (17), where N_t and N_B are the numbers of interior and boundary collocation points, respectively; $\left(x_t^j, y_t^j\right)$ and $\left(x_B^i, x_B^i\right)$ denote the coordinates of interior and boundary points; $h^{(1)}$ is the output of the first network layer; and C_0 is a boundary condition offset constant.

$$Loss_{\text{hard}} = \frac{1}{N_t}\sum_{j=1}^{N_t}\left|f\left[h^{(n)}\left(x_t^j, y_t^j, \vartheta\right)\right]\right|^2 + \frac{1}{N_B}\sum_{i=1}^{N_B}\left|h^{(1)}\left(x_B^i, x_B^i, \vartheta - C_0\right)\right|^2 \tag{17}$$

Under Python 3.7.5 and TensorFlow 1.14, a PINN surrogate was developed and trained to predict the synergy angles. The training was primarily driven by the operator residual $g(\phi) = 0$ as the core physical constraint, while inlet Dirichlet and wall Neumann boundary conditions were strictly enforced via a hard-constraint formulation. In addition, constraints associated with the k-ω SST turbulence model were incorporated, and CFD-extracted boundary synergy angle samples were used for supervised correction to improve convergence and predictive accuracy. The network adopted a fully connected architecture with four hidden layers, each containing 50 neurons, and used the Sigmoid activation function (see Figure 4a,b). A two-stage optimization strategy (Adam + L-BFGS-B) was employed: Adam was first used for pretraining (learning rate 1×10^{-3}, 2.0×10^4 iterations; other hyperparameters set to TensorFlow defaults) to obtain a stable initialization, after which a SciPy-based L-BFGS-B optimizer was applied for second-order refinement (maximum iterations 5.0×10^3). Convergence was declared when the relative change in the loss function fell below 10^{-8}. Interior collocation points were generated using Latin hypercube sampling (see Figure 4c), whereas boundary collocation points were generated by stratified random sampling. The numbers of collocation points were set to $N_t = 2.0 \times 10^4$ in the interior and $N_B = 5.0 \times 10^3$ on the boundaries (covering the inlet and the upper/lower walls). Insufficient baseline data may limit the performance and optimization of PINN models [29]. To overcome this limitation, a Generative Adversarial Network–Support Vector Machine (GAN-SVM) framework is employed to generate high-quality synthetic datasets, thereby enriching the original dataset and enhancing the model's generalization capability and predictive accuracy (see Figure 4d). The model is trained using the following hyperparameters: first- and second-order momentum decay rates of 0.999, an initial learning rate of 1×10^{-4}, and a learning rate decay factor of 0.999. Mini-batch training was adopted with batch sizes of 4096 (interior) and 1024 (boundary), while maintaining N_t:$N_B \approx$ 4:1 to balance the physics-residual term and the boundary supervision term.

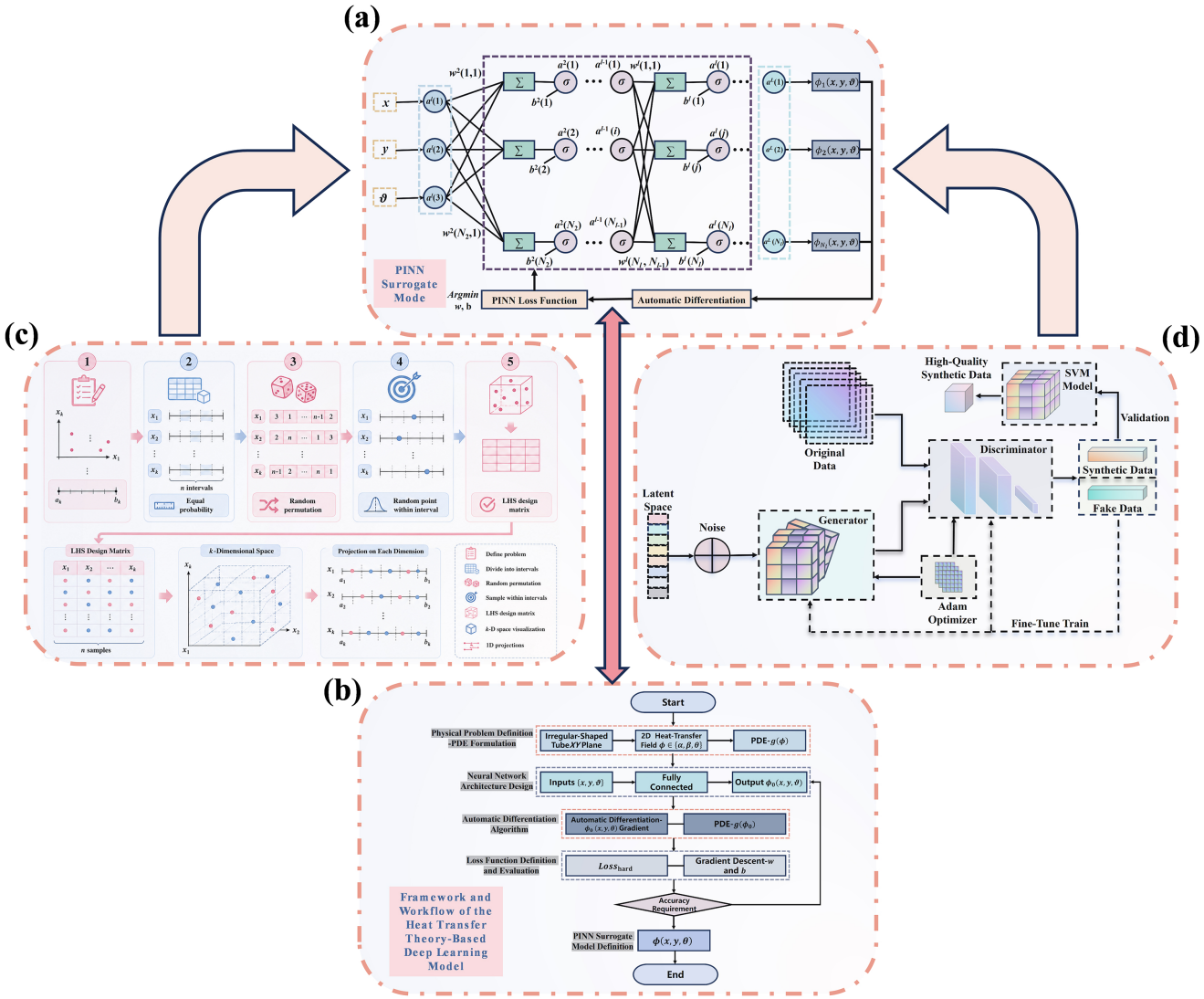


Figure 4. PINN workflow. (**a**) Fully connected network. (**b**) Physics constraints and training. (**c**) Interior and boundary sampling. (**d**) GAN–SVM data augmentation.

3. Results and Discussion

3.1. Multi-Field Synergy Theory Analysis

Figure 5 illustrates the vector relationships and overall synergy relationships of fluid particle M. According to the analysis of Figure 5a(i), when enhancing fluid heat transfer performance is the goal, the synergy between velocity U and temperature gradient ∇T should be prioritized. At this point, the smaller the synergy angle β, the higher the fluid heat transfer efficiency, resulting in an increase in the Nu. Conversely, when the goal is to reduce flow resistance, the synergy between velocity vector U and velocity gradient ∇u should be the focus. Here, the larger the synergy angle α, the smaller the momentum loss in the fluid, resulting in a reduction in pressure drop and lower drag coefficient f. Furthermore, the smaller the velocity gradient ∇u, the lower the fluid flow resistance, while the larger the temperature gradient ∇T, the stronger the heat transfer between the fluid and the inner wall. Figure 5a(ii) shows that when the synergy angle η remains constant, the smaller the synergy angle β, the larger the synergy angle θ, and vice versa. This indicates that for a given turbulence mode, enhancing heat transfer comes at the expense of increasing flow resistance, while reducing flow resistance weakens heat transfer. Figure 5a(iii) demonstrates

the three-dimensional physical vector synergy relationships of fluid particle M, where the synergy angles α, β, and θ between the velocity vector U and gradients ∇u, ∇T, and ∇p reflect the synergy degree of convective heat transfer characteristics, representing the direction of enhanced convective heat transfer, while the magnitudes $|U|$, $|\nabla u|$, $|\nabla T|$, and $|\nabla p|$ reflect the field intensity in convective heat transfer. In conclusion, these synergy angles reflect the synergistic laws between the velocity, temperature, and pressure fields. The momentum synergy angle α characterizes the directional relationship between the velocity vector and the velocity gradient-related momentum transport. As described in Section 2.1, α is mathematically related to the dot product $U \cdot \nabla u$, which corresponds to the convective acceleration term in the momentum equation. Therefore, α primarily provides information on the directional characteristics of momentum transport within the flow field. It should be noted that α is not directly equivalent to viscous flow resistance, because the viscous contribution in the momentum equation is associated with the viscous diffusion term rather than the convective acceleration term. In this study, α is therefore used to characterize the directional behavior of momentum transport, while the actual flow resistance characteristics are evaluated using the pressure drop and friction-related parameters obtained from the CFD results. The variation of α is discussed together with these macroscopic flow resistance parameters to analyze the relationship between the flow-field structure and flow resistance. In Figure 5b, A represents a mass flow micro-element with a normal vector as the velocity vector U; B represents a flow potential micro-element (isobaric surface) with a normal vector as the pressure gradient ∇p; and C represents a heat flux micro-element (isothermal surface) with a normal vector as the temperature gradient ∇T. Fluid particle M is located at the intersection of these three micro-element surfaces. Analysis reveals that there exists a competition between the synergy angles β and θ: when the velocity vector U aligns with the temperature gradient ∇T, the synergy angle β becomes smaller, favoring a reduction in thermal resistance. However, when the velocity vector U aligns with the pressure gradient ∇p, the synergy angle θ becomes smaller, helping reduce flow resistance. In Figure 5c, the dot product of velocity U and velocity gradient ∇u in the momentum synergy equation forms the synergy angle α; the dot product of velocity U and temperature gradient ∇T in the energy synergy equation forms the synergy angle β; the dot product of velocity U and pressure gradient ∇p in the mechanical energy synergy equation forms the synergy angle θ. Additionally, the angle between the velocity gradient ∇u and the temperature gradient ∇T is denoted as γ, and the angle between the temperature gradient ∇T and the pressure gradient ∇p is denoted as η.

To enhance heat transfer, the directions of mass flow and heat flow should be as aligned as possible, i.e., the synergy angle β should be as small as possible. From the perspective of reducing power consumption, the mass flow and driving force directions should align as much as possible, i.e., the synergy angle θ should be as small as possible. Finally, from the perspective of optimizing overall heat transfer performance, the synergy relationship between angles α, β, and θ should be optimized. In conclusion, the more optimal the synergy angles, the stronger the synergy effects, leading to a more significant enhancement in heat transfer.

The modified synergy angles α', β', and θ' can serve as fundamental metrics to evaluate enhanced heat transfer characteristics, where α' represents momentum transfer efficiency (flow resistance), β' represents heat transfer performance (thermal resistance), and θ' represents driving energy consumption (energy efficiency). Based on the modified synergy angles, two dimensionless comprehensive evaluation criteria are proposed: the performance evaluation coefficient (PEC') and the effectiveness evaluation coefficient (EEC'), as detailed in Equations (18) and (19). In these equations, the subscript 0 represents the smooth circular tube. By selecting "1/3" and "1/2" as exponents, based on engineering experience,

principles of convective heat transfer optimization in fluid dynamics, and mathematical optimization stability requirements, it is shown that the balance between flow and heat transfer is not symmetrical but tends to optimize heat exchange while minimizing flow loss.

$$PEC' = \frac{(\beta'/\beta_0')}{(\alpha'/\alpha_0')^{1/3}\cdot(\theta'/\theta_0')^{1/3}} \tag{18}$$

$$EEC' = \frac{(\beta'/\beta_0')\cdot(\alpha_0'/\alpha')^{1/2}}{(\theta'/\theta_0')} \tag{19}$$

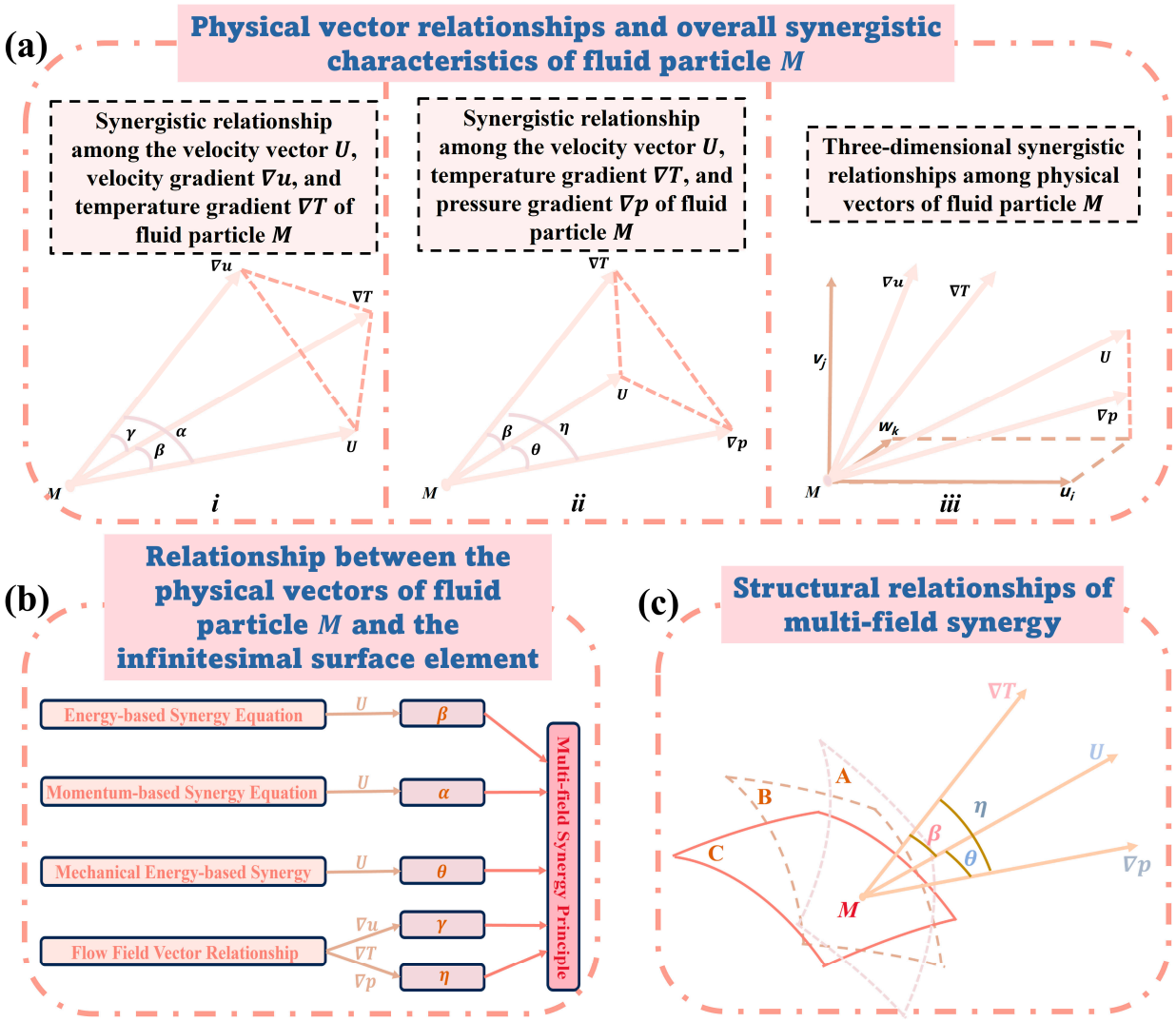


Figure 5. Multi-field synergy principles and structural relationships in convective heat transfer enhancement: (**a**) physical vector relationships and overall synergistic characteristics of fluid particle *M*; (**b**) relationship between physical vectors of fluid particle *M* and infinitesimal surface element; (**c**) structural relationships of multi-field synergy.

The subscript 0 denotes the smooth circular tube. *PEC*′ is used to characterize the comprehensive balance between heat transfer synergy and flow resistance characteristics, while *EEC*′ is used to further consider the combined effects of heat transfer, flow resistance, and power-consumption synergy. It should be noted that *PEC*′ and *EEC*′ are angle-based comprehensive evaluation criteria established in the present study. They are complementary to, rather than replacements for, the conventional performance evaluation criterion based

on the Nusselt number and friction factor. For reference, the conventional performance evaluation criterion is expressed in Equation (20).

$$PEC = \frac{Nu/Nu_0}{(f/f_0)^{1/3}} \tag{20}$$

where the exponent 1/3 is associated with the conventional equal-pumping-power evaluation condition. In contrast, the variables used in PEC' and EEC' are the synergy angles, which characterize the directional relationships among different physical field vectors. Therefore, the exponents 1/3 and 1/2 used in Equations (18) and (19) are not regarded as being directly derived from the conventional equal-pumping-power formulation. In the present study, they are retained as weighting parameters to balance the contributions of the corresponding angle-based terms in the proposed comprehensive evaluation criteria.

Accordingly, the conventional PEC based on Nu and f provides a benchmark for evaluating the overall heat transfer performance, whereas PEC' and EEC' provide complementary information from the perspective of multi-field synergy. The comparison of these indicators is therefore intended to examine the consistency between the conventional performance evaluation and the angle-based characterization, rather than to establish a mathematical equivalence between the two evaluation approaches.

The larger the PEC' value, the more significant the structural optimization effect, leading to a more effective balance between heat transfer enhancement, flow resistance, and energy consumption. The EEC' emphasizes evaluating the structural ability to maintain low energy consumption and low flow resistance while enhancing heat transfer performance. It accurately reflects the overall benefit of structural optimization, especially in balancing energy consumption and heat efficiency. Combining these two dimensionless evaluation criteria with the multi-field synergy principle framework allows for a comprehensive evaluation of the performance of different heat exchange tubes.

3.2. Multi-Field Synergy Pattern Analysis

This study uses the modified synergy angles α', β', and θ' as the primary evaluation metrics and employs PEC' and EEC' as the comprehensive evaluation criteria. The optimal parameter combination obtained by the PE and CADJ methods is as follows: tube diameter $d_{in} = 38.00$ mm, groove depth $e = 3.10$ mm, pitch $p = 25.23$ mm, air velocity $v = 5.30$ m·s^{-1}, inlet fluid temperature $T_{inlet} = 280.36$ K, and tube wall temperature $T_{wall} = 352.82$ K. Under these optimization conditions, the enhanced heat transfer characteristics of the helical groove tube, the novel-shaped tube, and the smooth circular tube are compared.

Figure 6a shows the differences in flow resistance characteristics for the three types of tubes.

Compared with the smooth circular tube, the irregular-shaped tube and the helical groove tube exhibit significantly increased energy consumption, which is associated with the flow disturbance induced by the spiral ribs. The standard α values indicate that the corresponding dot product between the velocity vector and the velocity gradient-related term can be negative in some regions, resulting in obtuse synergy angles and indicating an opposite directional relationship between the velocity vector and the velocity-gradient field. The modified α' values are obtained by taking the absolute value of the corresponding dot product; therefore, their smaller values relative to the standard α values in regions with obtuse standard angles are a mathematical consequence of the modified definition rather than an independent physical finding. In this study, the standard α is used to identify the directional characteristics associated with synergy and anti-synergy, whereas α' is used for quantitative comparison of different tube structures. This phenomenon reveals a locally antagonistic relationship between the velocity field and the velocity gradient in space, inhibiting the momentum diffusion capacity of fluid micro groups and altering the

momentum transport characteristics of the fluid. The average α' values for the irregular-shaped tube, the helical groove tube, and the smooth circular tube are 86.49°, 83.37°, and 89.57°, respectively. Compared with the helical groove tube, the irregular-shaped tube has a larger α' value and significantly lower flow resistance, indicating that the CADJ method can effectively reduce flow resistance (Equivalent contour maps are shown in Figure 7). Figure 6b reflects the thermal resistance of the three tube types. Compared with the smooth circular tube, the irregular-shaped tube and the helical groove tube exhibit significantly enhanced heat transfer performance due to the disturbance effect of the spiral ribs. The standard β values indicate that the velocity vector and temperature gradient field may exhibit opposite directional relationships in some regions, resulting in obtuse synergy angles. These regions are therefore identified as anti-synergy regions based on the standard formulation. The smaller β' values obtained from the modified formulation are a mathematical consequence of taking the absolute value of the corresponding dot product and should not be interpreted as an independent indication of an anti-synergy mechanism. Accordingly, the standard β is used to analyze the directional characteristics of thermal synergy and anti-synergy, while β' is used for quantitative comparison among different tube structures. This phenomenon reveals a locally antagonistic relationship between the velocity field and the temperature gradient in space, i.e., high-speed flow regions correspond to lower temperature gradients, inhibiting heat transfer and significantly weakening the synergistic enhancement effect of convective heat transfer. The average β' values for the irregular-shaped tube, the helical groove tube, and the smooth circular tube are 86.03°, 87.95°, and 89.87°, respectively. Compared with the helical groove tube, the irregular-shaped tube has a smaller β' value, indicating significantly superior heat transfer performance, demonstrating that the CADJ method can effectively enhance heat transfer (equivalent contour maps are shown in Figure 7). Figure 6c shows the energy consumption characteristics of the three tube types. Compared with the smooth circular tube, the irregular-shaped tube and the helical groove tube exhibit significantly increased energy consumption due to the disturbance effect of the spiral ribs. The standard θ values indicate that the velocity vector and pressure gradient field exhibit opposite directional relationships in some regions, resulting in obtuse synergy angles. These regions are identified as anti-synergy regions based on the standard formulation. The smaller θ' values are a mathematical consequence of taking the absolute value of the corresponding dot product and are therefore used for quantitative comparison rather than as direct evidence of an additional energy-saving mechanism. In this study, the standard θ is used to characterize the directional relationship between fluid motion and pressure driving, whereas θ' is used as a non-negative parameter for quantitative comparison among different tube structures. This phenomenon reveals a locally antagonistic relationship between the velocity field and the pressure gradient in space: high-speed flow regions correspond to lower pressure gradients, inhibiting mechanical energy transmission and leading to local flow resistance increase, thereby significantly improving energy-saving effects. The average θ' values for the irregular-shaped tube, the helical groove tube, and the smooth circular tube are 63.14°, 68.33°, and 17.17°, respectively. Compared with the helical groove tube, the irregular-shaped tube has a smaller θ' value and significantly lower energy consumption, indicating that the CADJ method can effectively reduce energy consumption (equivalent contour maps are shown in Figure 7).

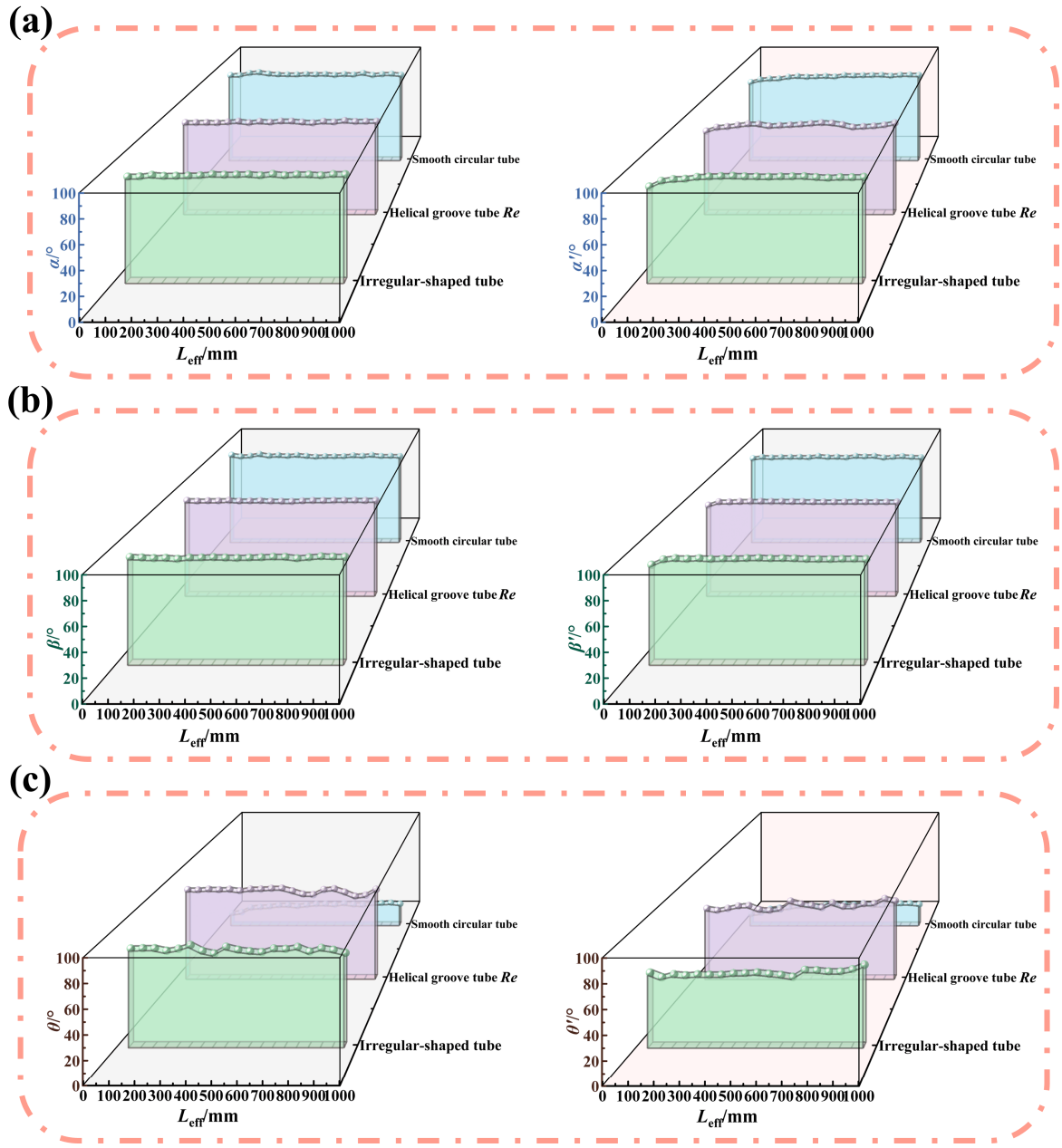


Figure 6. Spatial distribution characteristics of synergy angles for three tube geometries: (**a**) spatial distributions of α and α' values in mainstream direction; (**b**) spatial distributions of β and β' values in mainstream direction; (**c**) spatial distributions of θ and θ' values in mainstream direction.

It should be emphasized that the difference between the standard and modified synergy angles should be interpreted according to their mathematical definitions. When the corresponding vector dot product is negative, the standard synergy angle becomes obtuse ($90° < \gamma \leq 180°$), indicating an opposite directional relationship between the relevant physical field vectors. After taking the absolute value of the dot product, the modified angle is mathematically mapped into the range of 0–90°, with $\gamma' = 180 - \gamma$ for an original obtuse angle. Therefore, the smaller modified angles observed in comparison with the standard angles are a mathematical consequence of the modified formulation rather than an independent physical finding. In this study, the standard synergy angles are used to identify and analyze synergy and anti-synergy directional characteristics, whereas the modified synergy angles are used as non-negative parameters for quantitative comparison among different tube structures.

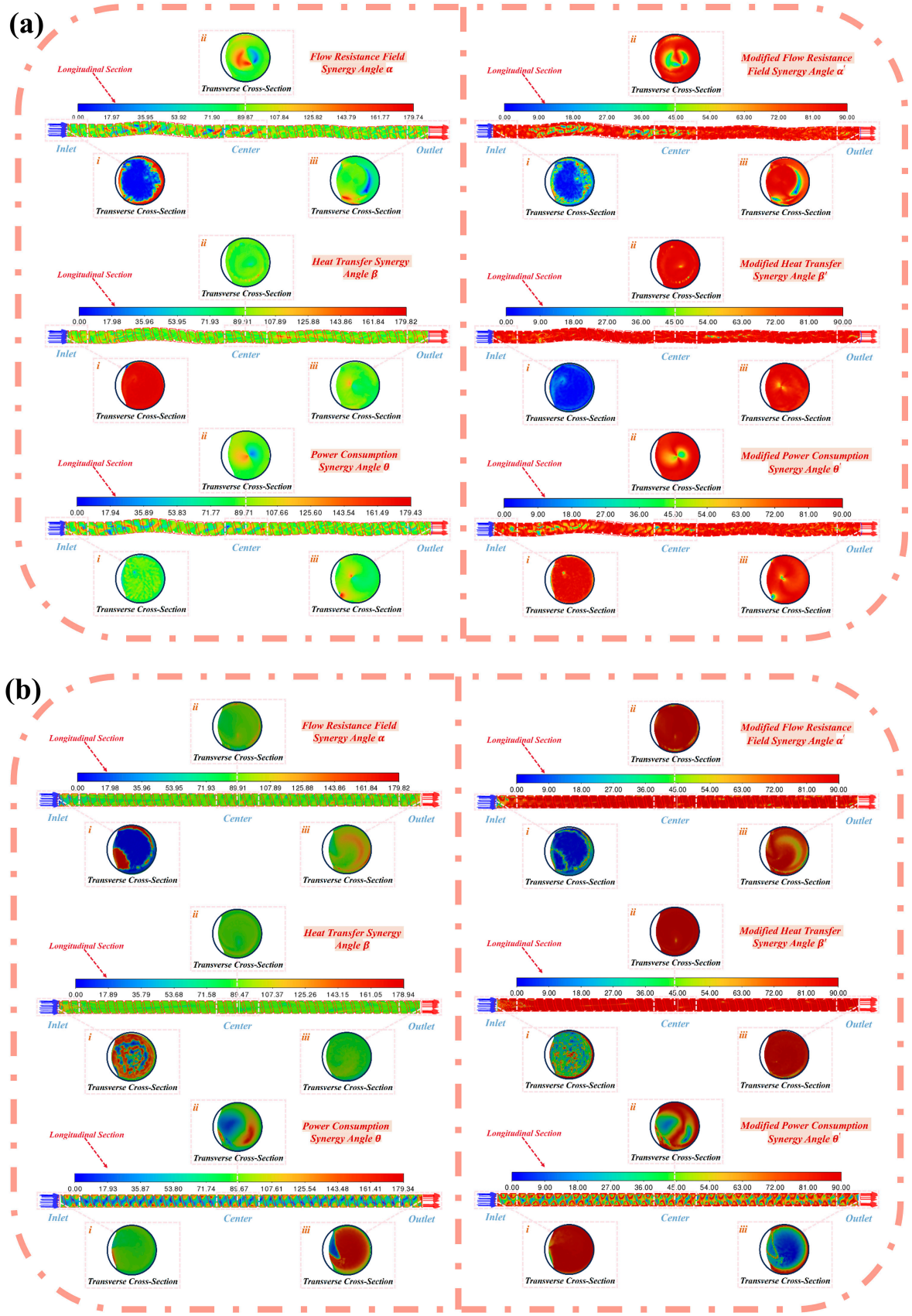


Figure 7. Contour maps of the standard and modified field synergy angles for two types of tubes in the *XY* longitudinal section and in multiple transverse cross-sections: (**a**) the irregular-shaped tube; (**b**) the helical groove tube.

3.3. Physics-Informed Neural Network Analysis

A single training iteration of the PINN model requires approximately 47.00 min. The model is trained for 500 cycles, and the best-performing result is selected. Given the large data volume of the generated cloud map of the field synergy angle, 500 coordinate points (i.e., 500 data samples) are randomly selected for error analysis against the CFD results. The predicted field synergy angle distribution and the corrected field synergy angle distribution are shown in Figures 8 and 9, respectively. The results indicate that the field synergy angle predicted by the model is in very close agreement with the simulation results and can accurately capture the variation trends arising from the coupling among different physical fields. Within the two-dimensional domain, the error generally remains on the order of 10^{-1}, with a mean error of 0.37° and a maximum relative error of 0.94°. These findings further demonstrate the high-accuracy performance of the proposed PINN model.

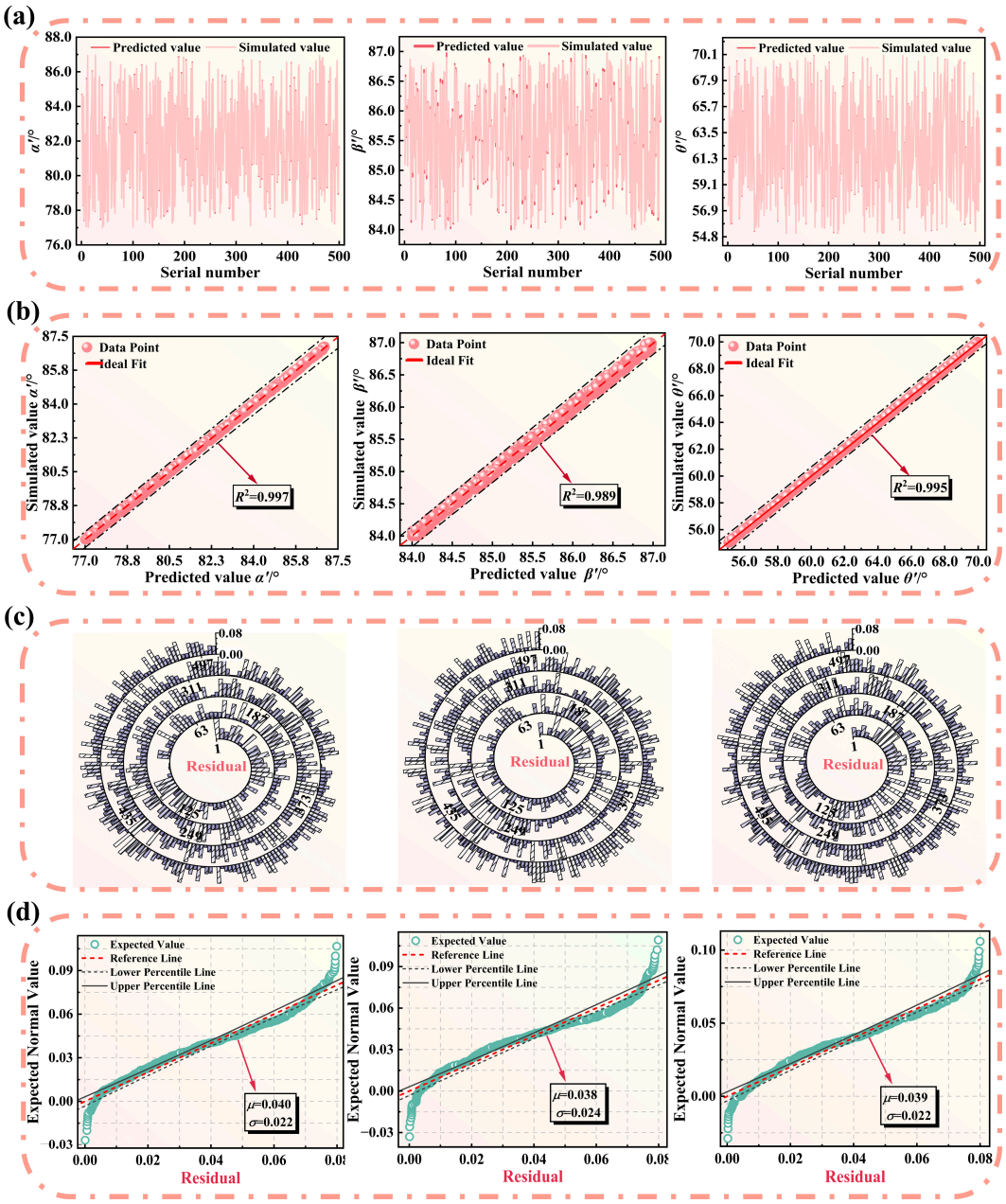


Figure 8. Predictive performance analysis (500 data groups): (**a**) predicted results; (**b**) goodness of fit; (**c**) residual distribution; (**d**) normal distribution of residuals.

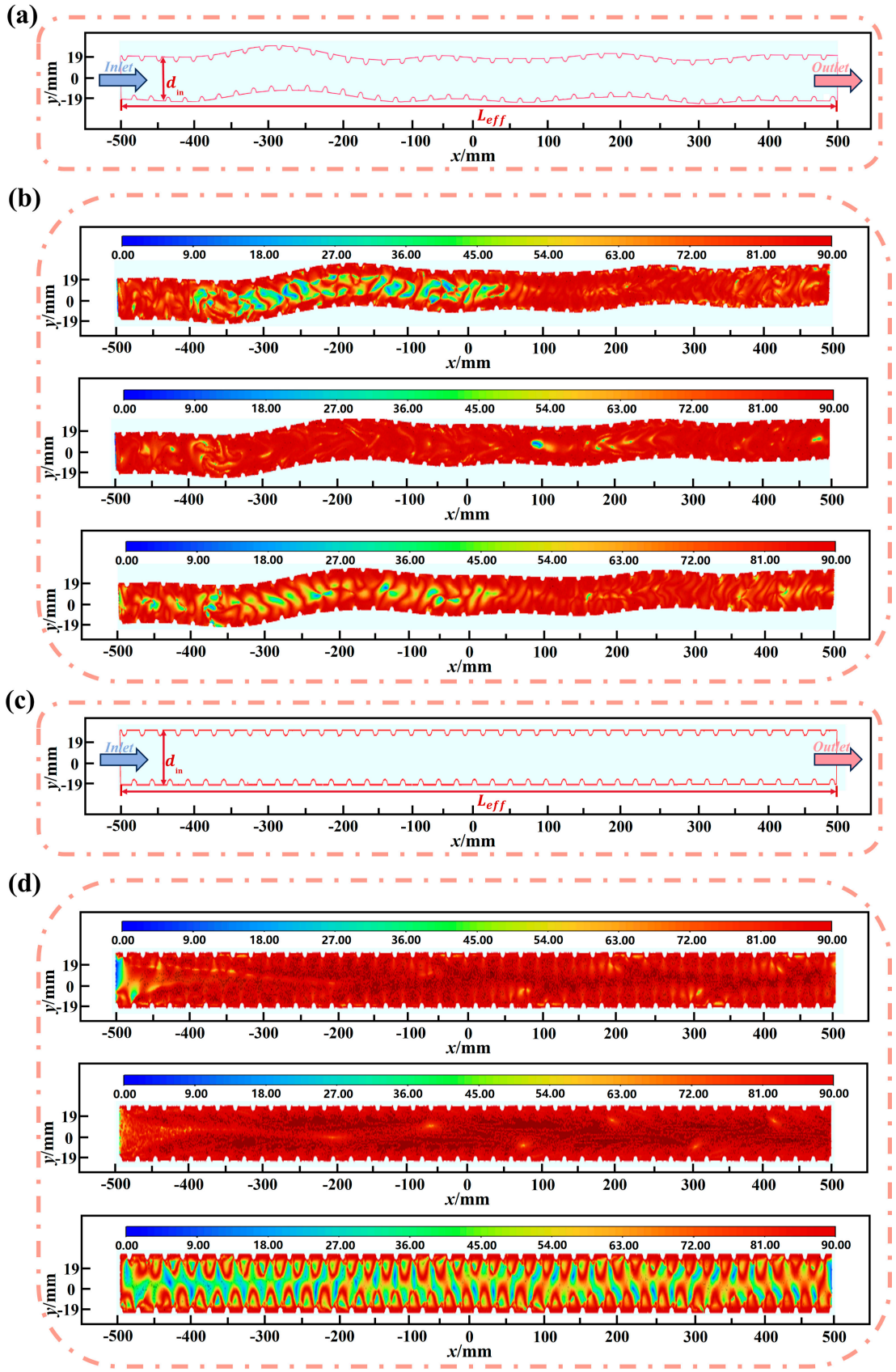


Figure 9. Analysis of the PINN surrogate model: (**a**) the two-dimensional physical model of the novel profiled tube; (**b**) the distribution of the field synergy angle for the novel profiled tube; (**c**) the two-dimensional physical model of the helical grooved tube; (**d**) the distribution of the field synergy angle for the helical grooved tube.

3.4. Comprehensive Performance Evaluation of the Heat Exchange Tube

In this study, since the *PEC*′ and *EEC*′ values range from 0.5 to 0.7 and 0.1 to 0.3, respectively, the classical "*PEC*′ > 1" and "*EEC*′ > 1" standards are not suitable for evaluating the enhanced heat transfer design in this study. Therefore, based on the synergy characteristics of convective enhanced heat transfer, the "optimization percentage" is used as the final evaluation criterion. The optimization percentage allows for a more reasonable quantification of the relative benefits of structural optimization, overcoming the limitations of using "1" as the standard. Figure 10a,b show the optimization percentage of the *PEC*′and *EEC*′ values for the irregular-shaped tube. Compared with the spatial distribution of *PEC*′and *EEC*′ values of the helical groove tube, the optimization percentage of the *PEC*′ value for the irregular-shaped tube is approximately 0.00–5.00%, while the optimization percentage of the *EEC*′ value is approximately 0.00–20.00%. Compared with the average *PEC*′ and *EEC*′ values of the helical groove tube, the average optimization percentage of the *PEC*′ value for the irregular-shaped tube is 2.03%, and the average optimization percentage of the *EEC*′ value is 7.82%. Therefore, this irregular-shaped tube significantly outperforms the helical groove tube in comprehensive heat transfer characteristics and is an efficient heat exchange tube.

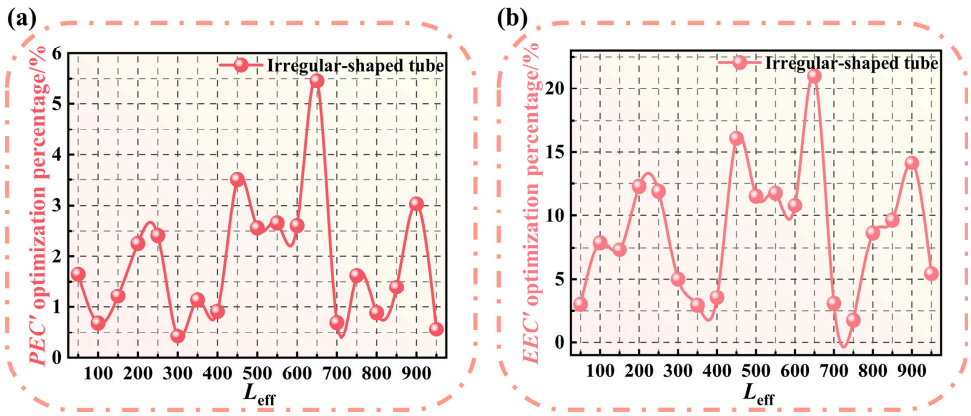


Figure 10. Optimization percentages of *PEC*′ and *EEC*′ for irregular-shaped tube: (**a**) optimization percentages of *PEC*′; (**b**) optimization percentages of *EEC*′.

In summary, by analyzing the physical vector relationships in the convective heat transfer flow field and constructing the corresponding synergy angles, the intrinsic link between synergy laws and enhanced heat transfer mechanisms can be revealed and mathematically expressed, thus establishing the multi-field synergy principle for convective enhanced heat transfer in theory. Based on this principle, the flow and heat transfer performance of different heat exchange units can be effectively evaluated.

It should be emphasized that the optimization percentages derived from the *PEC*′ and *EEC*′ represent the relative improvement calculated within the proposed angle-based evaluation framework. They should not be directly interpreted as the percentage improvement in the conventional *PEC*.

4. Conclusions

This paper, based on the conservation equations for momentum, energy, and mechanical energy, deeply analyzes the synergy of fluid particle physical vectors and reveals the intrinsic relationship between multi-field synergy laws and enhanced heat transfer mechanisms. A New Performance Evaluation Coefficient *PEC*′ and the Effectiveness Evaluation Coefficient *EEC*′ are proposed, and the application of multi-field synergy effects in enhanced

heat transfer in the helical groove tube and the irregular-shaped tube is systematically studied. The synergy effects are quantified, and their comprehensive heat transfer characteristics are evaluated. The research results indicate the following:

(1) The synergy angles α, β, θ, γ, and η reflect the multi-field synergy relationships in convective heat transfer. The more optimal the synergy angles, the higher the synergy degree and the better the heat transfer enhancement effect. The magnitudes of $|\nabla T|$, $|\nabla u|$, and $|\nabla p|$ represent the degree of enhanced heat transfer: the larger $|\nabla T|$, the lower the thermal resistance; and the smaller $|\nabla u|$ or $|\nabla p|$, the lower the flow resistance. Based on the multi-field synergy principle, a corresponding relationship exists between the synergy angles and the evaluation criteria for enhanced heat transfer, forming the theoretical foundation for convective heat transfer optimization.

(2) Standard synergy angles are suitable for studying enhanced heat transfer mechanisms and anti-synergy effects, while modified synergy angles are more suitable for optimization design and performance evaluation. The synergy angle α' represents momentum transfer efficiency (flow resistance), the synergy angle β' represents heat transfer performance (thermal resistance), and the synergy angle θ' represents driving energy consumption (energy efficiency). The larger the α' value and the smaller the β' and θ' values, and the lower the flow resistance, thermal resistance, and energy consumption of the heat exchange tube. The PEC' and EEC' reflect the heat transfer characteristics and energy efficiency performance of the heat exchange tube. The larger these values, the better the comprehensive performance of the heat exchange tube.

(3) The modified synergy angles of the three types of tubes are all smaller than the standard synergy angles, indicating significant anti-synergy effects in the fluid inside the tubes. Compared to the helical groove tube and the smooth circular tube, the irregular-shaped tube, based on the CADJ method, performs better in terms of flow resistance, heat transfer, and energy consumption. The average optimization percentages for the PEC' and EEC' values of the irregular-shaped tube are 2.03% and 7.82%, respectively, showing that it significantly outperforms the helical groove tube in comprehensive heat transfer characteristics and has higher heat transfer efficiency.

(4) In the absence of experimental validation, the field synergy angle reconstructed by the PINN exhibits an overall relative error on the order of 10^{-1} compared with the CFD results. This indicates that employing PINN to cross-validate and support the assessment of CFD predictions constitutes a simple and efficient alternative approach.

This study provides an angle-based framework for comparing internal flow and heat transfer in enhanced tubes. The results are limited to stationary single tubes with an effective length of 1000 mm, a uniform wall temperature, and the prescribed operating conditions. Shell-side flow, tube rotation, tube–bundle interactions, and nonuniform wall temperatures may influence performance at the exchanger scale. The interpretation of the two-dimensional PINN reconstruction is also limited by its use of CFD-derived boundary samples. In future work, we plan to fabricate the irregular-shaped tube by 3D printing and independently measure pressure drop, flow rate, and inlet and outlet temperatures. Particle image velocimetry (PIV) and spatial temperature measurements will help assess the local velocity and temperature fields used in the synergy angle analysis. Tests at additional operating points and with a full exchanger configuration would help determine how far the single-tube findings can be extended.

Author Contributions: Y.Z. and S.W.: Writing—review & editing, Writing—original draft, Conceptualization, Methodology, Data curation, Visualization, Validation, Formal analysis, Software. H.Z.: Visualization, Investigation, Software. L.W., C.W., G.C., H.W. and X.L.: Supervision, Resources, Funding acquisition. All authors have read and agreed to the published version of the manuscript.

Funding: This research was funded by the Natural Science Foundation of Heilongjiang Province [No. PL2026E028], the Natural Science Foundation of Heilongjiang Province [No. LH2022E098], the China Postdoctoral Science Foundation [No. 2024MD763975], the Heilongjiang Provincial Postdoctoral Science Foundation [No. LBH-Z24250], and the Heilongjiang Provincial Collaborative Innovation Achievement Project for Double First-Class Disciplines: Application of Intelligent Energy-Saving and Quality-Preserving Drying Technology for Raw Paddy Grain [No. LJGXCG2025-F22].

Data Availability Statement: Data will be made available on request.

Conflicts of Interest: The authors declare that they have no known competing financial interests or personal relationships that could have appeared to influence the work reported in this paper.

Nomenclature

c_p	Specific heat capacity (at constant pressure), J·(kg·K)$^{-1}$
d_{in}	Inner diameter of groove tube, mm
d_{out}	Outer diameter of helical groove tube, mm
e	Groove depth, mm
EEC'	Effectiveness evaluation coefficient, Dimensionless number
f	Darcy resistance coefficient, Dimensionless number
L_{eff}	Helical groove tube effective length, mm
$\dot{m}^{\text{n}}_{\text{inlet}}$	Inlet mass flow rate, kg·s^{-1}
n	Number of groove
Nu	Nusselt number, Dimensionless number
p	Pitch, mm
P_{outlet}	Gauge pressure, Pa
PEC'	Performance evaluation coefficient, Dimensionless number
Re	*Reynolds* number, Dimensionless number
$T^{\text{n}}_{\text{fluid}}$	Mainstream fluid temperature, K
T_{inlet}	Inlet fluid temperature, K
T_{wall}	Wall temperature, K
U	Flow velocity vector, m·s^{-1}
v	Air velocity, m·s^{-1}
V_x	Flow velocity x-vector, m·s^{-1}
V_y	Flow velocity y-vector, m·s^{-1}
V_z	Flow velocity z-vector, m·s^{-1}
w	Groove width, mm
y^+	Dimensionless wall distance
ΔP	Pressure loss, Pa
Δy	Distance from the first mesh layer to the wall, mm
∇p	Pressure gradient, Pa·m^{-1}
∇T	Temperature gradient, K·m^{-1}
∇u	Velocity gradient, s^{-1}
$\|U\|$	Flow velocity vector norm, m·s^{-1}
$\|\nabla p\|$	Pressure gradient norm, Pa·m^{-1}
$\|\nabla T\|$	Temperature gradient norm, K·m^{-1}
$\|\nabla u\|$ V	Velocity gradient norm, s^{-1}
Greek symbols	
α	Flow resistance synergy angle, °
α'	Modified flow resistance synergy angle, °
β	Heat transfer synergy angle, °
β'	Modified heat transfer synergy angle, °
β''	Helix angle, °
θ	Power consumption synergy angle, °
θ'	Modified power consumption synergy angle, °
λ	Thermal conductivity, W·(m·k)$^{-1}$
μ	Viscosity coefficient, N·s·m^{-2}
ρ	Fluid density, kg·m^{-3}
τ_{wall}	Wall shear stress, N·m^{-2}
$\partial T/\partial x$	Temperature x-gradient, K·m^{-1}
$\partial p/\partial x$ Pressure x-gradient, Pa·m^{-1}	$\partial p/\partial x$ Pressure x-gradient, Pa·m^{-1}
$\partial p/\partial y$ Pressure y-gradient, Pa·m^{-1}	$\partial p/\partial y$ Pressure y-gradient, Pa·m^{-1}
$\partial p/\partial z$ Pressure z-gradient, Pa·m^{-1}	$\partial p/\partial z$ Pressure z-gradient, Pa·m^{-1}

Superscript	
n Number	Number
Subscripts	
air	Air
eff	Effective
fluid	Fluid
in	Inner parameter
inlet	Inlet parameter
out	Outer parameter
outlet	Outlet parameter
p	Constant pressure condition
wall	Wall parameter

References

1. Kalendar, A.; Galal, T.; Al-Saftawi, A. Enhanced tubing thermal performance for innovative MSF system. *J. Mech. Sci. Technol.* **2011**, *25*, 1969–1977. [CrossRef]
2. Ahmad, H.E.; Mohammed, H.A.; Yosoff, M.Z. An overview on heat transfer augmentation using vortex generators and nanofluids: Approaches and applications. *Renew. Sust. Energy Rev.* **2012**, *16*, 5951–5993. [CrossRef]
3. Wu, J.X.; Wang, L.; Liu, Y.H. Research on film condensation heat transfer of the shell side of the spiral coil heat exchanger. *Int. J. Heat Mass Transf.* **2018**, *125*, 1349–1355. [CrossRef]
4. Wan, L.; Huang, Y.J.; Che, G.; Wang, H.C.; Li, J.P.; Zheng, Y.; Tian, J.K. Structural optimization and performance test of gas-phase rotating spiral grooved tube heat exchanger. *Trans. Chin. Soc. Agric. Mach.* **2024**, *55*, 422–432. (In Chinese)
5. Guo, Z.Y. Principle of field coordination in heat exchangers and its applications. *Chin. J. Mech. Eng.* **2003**, *39*, 1–9. (In Chinese) [CrossRef]
6. Tao, W.Q.; He, Y.L. Field synergy principle and its applications in enhancing convective heat transfer and improving performance of pulse tube refrigerator (1). *J. Xi'an Jiaotong Univ.* **2022**, *36*, 1101–1105. (In Chinese)
7. He, Y.L.; Tao, W.Q. Field synergy principle and its applications in enhancing convective heat transfer and improving performance of pulse tube refrigerator (2). *J. Xi'an Jiaotong Univ.* **2022**, *36*, 1106–1110. (In Chinese)
8. Meng, J.A.; Liang, X.G.; Li, Z.X. Field synergy optimization and enhanced heat transfer by multi-longitudinal vortices flow in tube. *Int. J. Heat Mass Transf.* **2005**, *48*, 3331–3337. [CrossRef]
9. Kuo, J.K.; Chen, C.K. Evaluating the enhanced performance of a novel wave-like form gas flow channel in the PEMFC using the field synergy principle. *J. Power Sources* **2006**, *162*, 1122–1129. [CrossRef]
10. Chen, C.K.; Yen, T.S.; Yang, Y.T. Lattice Boltzmann method simulation of a cylinder in the backward-facing step flow with the field synergy principle. *Int. J. Therm. Sci.* **2006**, *45*, 982–989. [CrossRef]
11. Ma, L.D.; Li, Z.Y.; Tao, W.Q. Experimental verification of the field synergy principle. *Int. J. Heat Mass Transf.* **2006**, *34*, 269–276. [CrossRef]
12. Tao, Y.B.; He, Y.L.; Huang, J.; Wu, Z.G.; Tao, W.Q. Three-dimensional numerical study of wavy fin-and-tube heat exchangers and field synergy principle analysis. *Int. J. Heat Mass Transf.* **2006**, *50*, 1163–1175. [CrossRef]
13. Tao, Y.B.; He, Y.L.; Wu, Z.G.; Tao, W.Q. Three-dimensional numerical study and field synergy principle analysis of wavy fin heat exchangers with elliptic tubes. *Int. J. Heat Fluid Flow* **2007**, *28*, 1531–1544. [CrossRef]
14. Chen, Q.; Ren, J.X.; Meng, J.A. Field synergy equation for turbulent heat transfer and its application. *Int. J. Heat Mass Transf.* **2007**, *50*, 5334–5339. [CrossRef]
15. Wu, J.M.; Tao, W.Q. Investigation on laminar convection heat transfer in fin-and-tube heat exchanger in aligned arrangement with longitudinal vortex generator from the viewpoint of field synergy principle. *Appl. Therm. Eng.* **2007**, *27*, 2609–2617. [CrossRef]
16. Cheng, Y.P.; Lee, T.S.; Low, H.T. Numerical simulation of conjugate heat transfer in electronic cooling and analysis based on field synergy principle. *Appl. Therm. Eng.* **2007**, *28*, 1826–1833. [CrossRef]
17. Wu, J.M.; Tao, W.Q. Numerical study on laminar convection heat transfer in a rectangular channel with longitudinal vortex generator, Part A: Verification of field synergy principle. *Int. J. Heat Mass Transf.* **2007**, *51*, 1179–1191. [CrossRef]
18. Chang, C.C.; Yang, Y.T.; Yen, T.H.; Chen, C.K. Numerical investigation into thermal mixing efficiency in Y-shaped channel using Lattice Boltzmann method and field synergy principle. *Int. J. Therm. Sci.* **2009**, *48*, 2092–2099. [CrossRef]
19. Guo, J.F.; Xu, M.T.; Cheng, L. The application of field synergy number in shell-and-tube heat exchanger optimization design. *Appl. Energy* **2009**, *86*, 2079–2087. [CrossRef]

20. Gou, C.H.; Cai, R.X.; Liu, Q.B. Field synergy analysis of laminar forced convection between two parallel penetrable walls. *Int. J. Heat Mass Transf.* **2009**, *52*, 1044–1052. [CrossRef]
21. Guo, J.F.; Xu, M.T.; Cheng, L. Numerical investigations of circular tube fitted with helical screw-tape inserts from the viewpoint of field synergy principle. *Chem. Eng. Process.* **2010**, *49*, 410–417. [CrossRef]
22. Li, J.; Ling, X.; Peng, H. Field synergy analysis on convective heat transfer and fluid flow of a novel triangular perforated fin. *Int. J. Heat Mass Transf.* **2013**, *64*, 526–535. [CrossRef]
23. Hua, Y.C.; Zhao, T.; Guo, Z.Y. Optimization of the one-dimensional transient heat conduction problems using extended entransy analyses. *Int. J. Heat Mass Transf.* **2018**, *116*, 166–172. [CrossRef]
24. Mehra, B.; Simo Tala, J.V.; Habchi, C.; Harion, J.L. Local field synergy analysis of conjugate heat transfer for different plane fin configurations. *Appl. Therm. Eng.* **2018**, *130*, 1105–1120. [CrossRef]
25. Zhang, Y.; Zhang, X.; Li, M.; Liu, Z. Research on heat transfer enhancement and flow characteristic of heat exchange surface in cosine style runner. *Heat Mass Transf.* **2019**, *55*, 3117–3131. [CrossRef]
26. Zuo, Q.; Li, Q.; Yang, X.; Chen, W.; Zhu, G.; Shen, Z.; Xie, Y.; Tang, Y. Investigation of electrically heating catalytic converter flow and temperature field performance improvement based on field synergy. *Energy* **2023**, *274*, 127360. [CrossRef]
27. Hao, J.; Chen, J.; Ma, T.; Hao, T.; Zhou, J.; Du, X. Flow channel structure optimization and analysis of proton exchange mem-brane fuel cell based on the finite data mapping and multi-field synergy principle. *Int. J. Heat Mass Transf.* **2023**, *207*, 123997. [CrossRef]
28. Liu, W.; Liu, Z.; Ma, L. Application of a multi-field synergy principle in the performance evaluation of convective heat transfer enhancement in a tube. *Chin. Sci. Bull.* **2012**, *57*, 1600–1607. [CrossRef]
29. Hou, T.; Xu, H.; Jin, F. Heat transfer performance of microchannels with elliptic cavities based on field synergy principle and entropy production analysis. *Int. Commun. Heat Mass Transf.* **2025**, *166*, 109174. [CrossRef]
30. Wei, C.; Zhang, H.; Xu, J. Optimizing direct contact heat exchangers via topological approach: Multi-field synergy analysis to flow and heat transfer. *Appl. Therm. Eng.* **2025**, *276*, 126824. [CrossRef]
31. Zhang, F.; Wang, J.; Qian, C. Performance comparison and analysis of gradient-optimized triply periodic minimal surface heat exchangers based on field synergy principle. *Appl. Therm. Eng.* **2025**, *275*, 126887. [CrossRef]
32. Qian, C.; Wang, J.; Qiu, X. Optimization design and heat transfer investigation of TPMS compact heat exchanger based on field synergy principle. *Int. Commun. Heat Mass Transf.* **2025**, *165*, 109003. [CrossRef]
33. Chua, Y.Y.A.M.; Kumar, P.; Shah, T.M. Computational study of helical coil heat exchanger: Energy, entropy, exergy, entransy (4E) analysis and application of field synergy principle. *Int. J. Refrig.* **2025**, *172*, 41–63. [CrossRef]
34. Shi, D.; He, L.Y.; Wang, S. Optimization design of flow path arrangement and channel structure for lithium-ion battery cooling plate based on the three-field synergy principle. *Appl. Therm. Eng.* **2025**, *264*, 125372. [CrossRef]
35. Pan, W.; Wang, S.; Huang, T. Effect of screw design on the mixing and heat efficiencies in an extrusion system by tailoring ductile forming with field synergy principle. *Appl. Therm. Eng.* **2025**, *262*, 125291. [CrossRef]
36. Wei, C.; Zhang, H.; Xu, J. Flow and heat transfer analysis of direct contact heat exchanger based on the multi-field synergy principle. *Int. Commun. Heat Mass Transf.* **2025**, *161*, 108553. [CrossRef]
37. Tong, X.Z. A local synergy angle of velocity, temperature and pressure fields for enhancement of comprehensive heat transfer performance. *Case Stud. Therm. Eng.* **2024**, *64*, 105466. [CrossRef]
38. Zhang, F.; Tao, J.; Gou, H. Thermal performance analysis of a novel letter-type fin liquid cooling plate based on the field synergy principle and the second law of thermodynamics. *Therm. Sci. Eng. Prog.* **2024**, *56*, 103027. [CrossRef]
39. Hou, T.; Lin, S.; Tu, Z. Heat transfer performance of microchannels with different reentrant cavities based on field synergy principle and entropy production analysis. *Int. Commun. Heat Mass Transf.* **2024**, *158*, 107851. [CrossRef]
40. Wang, S.; Wan, L.; Che, G.; Wang, H.C.; Du, T.B.; Diao, X.Q. Experimental study and motion parameter optimization of the shell side of a gas-phase rotating shell-and-tube heat exchanger based on an improved NSGA-II algorithm. *Int. J. Heat Fluid Flow* **2025**, *116*, 109952. [CrossRef]
41. Wang, S.; Wan, L.; Wang, H.C.; Che, G.; Li, Y.; Du, T.B.; Wang, C.F. The optimized design and heat transfer characteristics of helical groove tubes: A study based on parameter estimation, continuous adjoint optimization, and physics-informed neural networks. *Int. J. Heat Fluid Flow* **2026**, *119*, 110251. [CrossRef]
42. Wang, S.; Wan, L.; Che, G.; Wang, H.C.; Du, T.B.; Wang, C.F. Numerical investigation of secondary flow-induced heat transfer enhancement mechanisms and near-wall flow structures in helical groove tubes. *Appl. Therm. Eng.* **2025**, *279*, 128002. [CrossRef]
43. Nichols, R.H.; Nelson, C.C. Wall function boundary conditions including heat transfer and compressibility. *AIAA J.* **2004**, *42*, 1107–1114. [CrossRef]
44. Menter, F.R. Review of the shear-stress transport turbulence model experience from an industrial perspective. *Int. J. Comput. Fluid Dyn.* **2009**, *23*, 305–316. [CrossRef]

45. Zhang, D.S.; Wu, S.Q.; Shi, W.D.; Pan, D.Z.; Yao, J.; Zhang, G.J. Application and experiment of different turbulence models for simulating tip leakage vortex in axial flow pump. *Trans. Chin. Soc. Agric. Eng.* **2013**, *29*, 46–53. [CrossRef]
46. Wang, S.; Wan, L.; Wang, H.C.; Che, G.; Li, Y.; He, S.G.; Du, Q.Q.; Fan, L.Z. Study on the relationship between secondary flow intensity and synergy effects in the helical groove tube: A multiscale analysis of flow-heat synergy. *Int. Commun. Heat Mass Transf.* **2026**, *172*, 110647. [CrossRef]

Disclaimer/Publisher's Note: The statements, opinions and data contained in all publications are solely those of the individual author(s) and contributor(s) and not of MDPI and/or the editor(s). MDPI and/or the editor(s) disclaim responsibility for any injury to people or property resulting from any ideas, methods, instructions or products referred to in the content.